Top Hammer Drill Simulation in Varying Rock Conditions

Suvi Peltokangas
Automation and Hydraulic Engineering
Faculty of Engineering Sciences
Tampere, Finland
suvi.peltokangas@tuni.fi

Sirpa Launis
Sandvik Mining and Rock Technology
Tampere, Finland
sirpa.launis@sandvik.com

Markus Saarela
Sandvik Mining and Rock Technology
Tampere, Finland
markus.saarela@sandvik.com

Jouni Mattila
Automation and Hydraulic Engineering
Faculty of Engineering Sciences
Tampere, Finland
jouni.mattila@tuni.fi

***Abstract*—Rock breaking using a top hammer drill is achieved with a combination of four distinct hydraulically driven functions; percussion, feed, rotation and flushing the hole. Percussion, feed and rotation are applied to the drill string outside the drill hole. Flushing water or another flushing medium is pumped through the drill string to the bit. Controlling top hammer drill rigs in varying rock conditions is an important task, as non-optimal control can damage drilling equipment and waste energy. Damage occur especially when percussion-induced stress waves are not optimally transmitted to the rock and are thus reflected from the drill bit–rock interface to the drill. Therefore, to design an adaptive control system to manage drilling in all rock conditions, it is meaningful to develop a simulator that can produce data comparable to real-life drilling. This paper presents a rock drill simulator designed in MATLAB/Simulink environment. The rock drill model has hydraulic feed and rotation circuits, and drill string is modeled as a finite element beam having three degrees of freedom per node and two nodes per element. A total of 90 elements were used for the drill string modeling. The simulation also includes a rock model that can be modified to emulate varying rock conditions. By modifying the parameters of the rock model and boundary conditions, penetration rate changes and the simulated strain from the drill string varies.**

Keywords—Top hammer drill, stress wave, rock model, simulation.

I. Introduction

Modern lifestyles have created a growing need for efficient ore extraction. One method for ore extraction is drilling and blasting in underground mines. Nowadays, blasthole drilling is mainly done with hydraulic drilling rigs. Pneumatic rock drills found a competitor when hydraulic percussive drills were introduced in the early 1970s [1]. These new rock drills doubled rock drilling capacities compared with pneumatic drills. Hydraulic top hammer drills mainly use impact energy for rock breaking; however, reasonable parameter values for feed, rotation and flushing in relation to percussion power are also needed for efficient drilling. The output power of the percussion circuit depends on both pressure and the flow rate. To ensure that the drill bit remains attached to the rock, the feed force must be sufficient. The bit is rotated between blows to provide fresh rock under the bit buttons. [1] Hydraulic rock drilling has led to enhancements in drilling accuracy and automation. However, there is still a need for adaptive control in varying rock conditions.

Hydraulic percussive drilling has been widely studied over the past few years [2]–[11]. Most studies have concentrated on rock mechanics and the modeling of impulsive forces in the bit–rock interactions. However, in these studies, either the drill models are focused on a single percussive blow or the rock models are very complex. Impulsive forces exerted on the drill rod outside the hole generate rapid stress waves. These waves travel through the drill string to the drill bit and should be transmitted to the rock as efficiently as possible. Otherwise, regenerative reflected forces can cause damage to the drilling equipment and loss of energy. Effective stress wave transmission can be achieved by controlling the percussion cylinder stroke length or frequency, which typically is about 100 Hz, along with the feed and rotation parameters. The challenge of implementing such control is that the mobile hydraulic valve-controlled feed and rotation circuits have rather slow dynamics, in the order of a few hertz.

Pettersson [12] constructed a multi-domain simulation model of a hydraulic rock drill divided into five parts: a rock drill machine model, a rod model, a penetration model, a loading system model and a supply system model. Stress-wave propagation in the rod was studied through analogies to a transmission line and described as a four pole equation. However, study did not concentrate on the stress wave shapes at varying rock conditions.

Drill string models are introduced especially in the case of drilling boreholes in oil and gas industry [13], [14], where, penetration into the rock is achieved by the rotary motion only. Aarsnes and Wouw [13] modelled the bit–rock interaction to include cutting and frictional effects.

In this study, the hydraulic feed and rotation circuits of hydraulic rotary–percussive drilling were modelled. Information about percussion was used both for the rock model to estimate the penetration rate and for the simulation of the stress wave generation in the drill string. Rock was modelled as a mass–damper system with additional parameters to roughly estimate the drill's the penetration rate. Flushing is presumed to be sufficient for this simulation. The drill string was modeled as a Euler–Bernoulli beam with two–node elements and three degrees of freedom per node: forward/backward, up/down and roll. A total of 90 elements were used for the drill string modeling. Stress wave shapes under varying boundary conditions were illustrated and compared with real stress wave measurements. The goal was

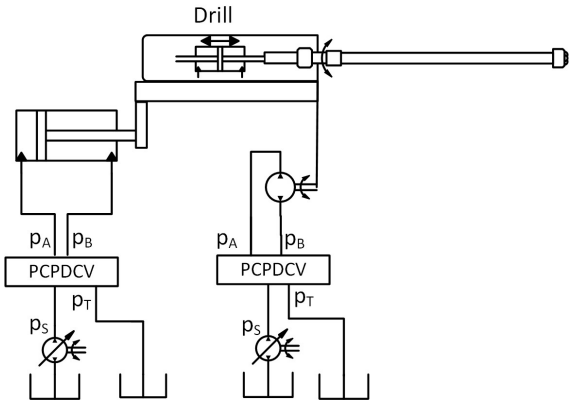

Fig. 1. Diagram of the feed and rotation functions of a hydraulic drill [15]

to develop a drilling simulator for testing different control system designs under varying rock conditions.

II. Modeling of Drill Functions

The feed and rotation circuits of the top hammer drill were modelled as in [15]. Both circuits have a pressure-compensated proportional directional control valve (PCPDCV) and a variable displacement pump, as illustrated in Fig. 1. A hydraulic circuit of a PCPDCV is shown in Fig. 2. Rotation of the drill rod is achieved with the use of a constant displacement motor, and pressure is controlled with pressure reducing valves (PRVs)

A. Axial Piston Pump

The axial piston pump is controlled by a constant pressure control strategy. The pump produces flow Q_P as follows:

$$Q_P = n_P V_P \varepsilon - C_P p_S \tag{1}$$

where n_P is the rotational speed (rad/s), V_P is the pump volumetric displacement (m3/rad), ε is the pump angle [0...1], C_P is the leakage coefficient [m3/(s·Pa)], and p_S is the pump supply pressure (Pa). The pump angle is a function of the pressure difference between the requested supply pressure p_{RS} and the supply pressure p_S [16]–[18].

$$\varepsilon = (\tau_1 s + 1)(p_{RS} - p_S) / (\tau_2 s + 1) \tag{2}$$

where time constants τ_1, and τ_2 define the dynamics between the pump angle and the pressure difference. The derivative of the pump feed pressure is

$$\dot{p}_S = B_H (Q_P - Q_{LS} - Q_H) / V_H \tag{3}$$

where B_H and V_H are the bulk modulus and the volume of the pressure line, respectively, Q_{LS} is the flow to an actuator, and Q_H is the flow to the pressure relief valve.

B. Pressure Compensator

Changes in the load pressure cause a variable flow rate through the valve without pressure compensation. The pressure-compensated valve changes its opening to maintain a constant flow rate. The opening of the pressure compensator is defined as follows [19]:

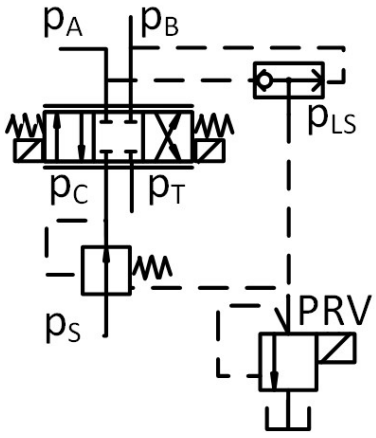

Fig. 2. Hydraulic diagram of the PCPDV valve. [15]

$$u_C = (p_{LS} + p_0 + K_C - p_C)/K_C \tag{4}$$

where p_{LS} is the load pressure (Pa), p_0 is the pre-compression pressure of the pressure compensator spring (Pa), K_C is the normalized spring stiffness (Pa), and p_C is the compensated pressure (Pa). The opening of the pressure compensator u_C is dimensionless and is limited to the interval [0,1].

The flow through the valve can be either laminar or turbulent. To achieve a smooth transition between laminar and turbulent flow, the formula proposed by Ellman and Piché [20] is used in this simulator. The flow through the pressure compensator is

$$Q_C = \begin{cases} |p_S - p_C| \sqrt{|p_S - p_C|} C_C u_C & \text{for } |p_S - p_C| \geq p_{TR} \\ \frac{C_C u_C |p_S - p_C|}{2\sqrt{p_{TR}}} \left(3 - \frac{|p_S - p_C|}{p_{TR}}\right) & \text{for } |p_S - p_C| < p_{TR} \end{cases} \tag{5}$$

where p_{TR} is the pressure limit, which determines the flow type as either turbulent or laminar, and C_C is the flow coefficient of the valve.

The pressure differential $\dot{p}_C$ can be calculated as

$$\dot{p}_C = B_{eff} (Q_C - Q_{LS})/V_{pc} \tag{6}$$

where B_{eff} is the bulk modulus, V_{pc} is the volume between the pressure compensator and the directional valve, and Q_{LS} is the flow to the load [19].

The load pressure p_{LS} is controlled by the PRV, and it is inputted into (4). In this simulation, the Lookup Table Dynamic block is used to model the valve opening area. The inputs to the block are the pressure values for the initial, full and saturation opening, and the output is the valve opening area. The valve opening area is zero before the initial opening pressure is reached. The opening area then grows linearly until reaching full area when full opening pressure is reached. The flow into the tank is determined using (5).

C. Proportional Directional Valve

In this simulation, the proportional directional valves for both modelled hydraulic circuits are 4/3 spool valves. The flow through a flow channel depends on the pressure difference across the flow path and is calculated as

$$Q(p_1, p_2) = \begin{cases} |p_1 - p_2| \sqrt{|p_1 - p_2|} K_v u & \text{for } |p_1 - p_2| \geq p_{TR} \\ \frac{K_v u |p_1 - p_2|}{2\sqrt{p_{TR}}} \left(3 - \frac{|p_1 - p_2|}{p_{TR}}\right) & \text{for } |p_1 - p_2| < p_{TR} \end{cases} \tag{7}$$

where Kv and u are the flow coefficient and the opening of the valve, respectively. The value of the u is limited to the interval [0,1], and $|p_1 - p_2|$ is the absolute pressure difference across the flow path [20]. In this simulation, the 4/3 proportional directional spool valves consist of four different flow paths: two flow paths from the pump side of the valve to the load and two flow paths back to the tank. The flows to the load are presented as

$$Q_A = Q(p_P, p_A) - Q(p_A, p_T) \quad (8a)$$

$$Q_B = Q(p_P, p_B) - Q(p_B, p_T) \quad (8b)$$

where p_P is the pressure on the pump side of the valve, p_A is the pressure on the actuator side A, p_T is the tank pressure, p_B is the pressure on the actuator side B, and $Q(.,.)$ is a flow through a flow path defined in (7).

The dynamics between the valve control and the spool position in the Simulink environment are modeled by connecting the delay and the rate limiter blocks in a series. There is a static non-linear function between the opening u of each flow channel and the spool position. This function defines the valve lap; valves can be classified as zero-lapped, underlapped, or overlapped.

D. Motor

The motor of the rotation circuit is a constant displacement motor without external leakage. Thus, the volume flow out of the motor Q_M is calculated as

$$Q_M = V_M n_M + C_M \Delta p \quad (9)$$

where V_M is the theoretical volumetric displacement of the motor (m3/rad), n_M is the rotational speed of the motor (rad/s), $\Delta p = p_A - p_B$ is the pressure difference in the motor ports, and C_M is the motor leakage coefficient [m3/(s·Pa)]. The torque of the motor axle T_M is modelled as

$$T_M = \Delta p V_M. \quad (10)$$

The pipes from the valve to the motor and from the motor to the valve are modelled as volumes and denoted as V_a and V_b, respectively. The pressure differentials at the motor ports A and B are calculated with (11a) and (11b).

$$\dot{p_A} = \frac{B_{eff}}{V_a}(Q_A - Q_M) \quad (11a)$$

$$\dot{p_B} = \frac{B_{eff}}{V_b}(Q_M + Q_B) \quad (11b)$$

where B_{eff} is the effective bulk modulus, and the positive flow direction for Q_B is from the valve to the motor.

E. Feed

The feed actuator is a double-acting single-rod cylinder (70/50-2700). The pressure differentials on the sides A and B of the cylinder are calculated with (12a) and (12b).

$$\dot{p_A} = \frac{B_{eff}}{A_A x_c + V_{0A}}(Q_A - \dot{x}_c A_A) \quad (12a)$$

$$\dot{p_B} = \frac{B_{eff}}{A_B (L - x_c) + V_{0B}}(Q_B + \dot{x}_c A_B) \quad (12b)$$

where A_A, A_B are the areas of the piston sides A and B respectively, x_c and $\dot{x}_c$ are the position and velocity of the piston, respectively, L is the cylinder stroke, and V_{0A} and V_{0B} are dead volumes on the cylinder sides A and B, respectively [20].

Cylinder friction is included in the force equation of the cylinder. Canudas de Wit et al. [21] modelled the steady-state motion relation between velocity and friction force as

$$F_{ss}(\dot{x}_c) = F_C \operatorname{sgn}(\dot{x}_c) + (F_S - F_C) e^{-(\dot{x}_c / v_s)^2} \operatorname{sgn}(\dot{x}_c) + \sigma_2 \dot{x}_c \quad (13)$$

where F_C is the Coulomb friction level, F_S is the stiction force level, v_s is the Stribeck velocity, and σ_2 is the viscous friction parameter. The signum function is denoted by sgn().

III. Beam Model

The drill string is modeled as a finite element beam with three degrees of freedom per node, as illustrated in Fig. 3. The forces acting on the beam are axial force, shear force and torsional moment. The local stiffness matrix for the ith beam element is given as

$$[k^i_{local}] = \begin{bmatrix} \frac{AE}{L} & 0 & 0 & \frac{-AE}{L} & 0 & 0 \\ 0 & \frac{12EI}{L^3} & 0 & 0 & \frac{-12EI}{L^3} & 0 \\ 0 & 0 & \frac{G}{JL} & 0 & 0 & \frac{-G}{JL} \\ \frac{-AE}{L} & 0 & 0 & \frac{AE}{L} & 0 & 0 \\ 0 & \frac{-12EI}{L^3} & 0 & 0 & \frac{12EI}{L^3} & 0 \\ 0 & 0 & \frac{-G}{JL} & 0 & 0 & \frac{G}{JL} \end{bmatrix} \quad (14)$$

where A is the cross-sectional area of the beam, E is Young's modulus, L is the length of the element, I is the moment of inertia, G is the shear modulus and J is the cross-sectional polar moment of inertia. The local geometric stiffness matrix for the ith beam element is

$$[k^i_g] = N/L \begin{bmatrix} 1 & 0 & 0 & -1 & 0 & 0 \\ 0 & \frac{6}{5} & 0 & 0 & \frac{-6}{5} & 0 \\ 0 & 0 & 0 & 0 & 0 & 0 \\ -1 & 0 & 0 & 1 & 0 & 0 \\ 0 & \frac{6}{5} & 0 & 0 & \frac{-6}{5} & 0 \\ 0 & 0 & 0 & 0 & 0 & 0 \end{bmatrix} \quad (15)$$

where N is axial force.

The transformation matrix between the local and global coordinate system is

$$[t] = \begin{bmatrix} \cos(\theta) & \sin(\theta) & 0 \\ -\sin(\theta) & \cos(\theta) & 0 \\ 0 & 0 & 1 \end{bmatrix} \quad (16)$$

where θ is the angle between the local and global coordinate axes.

The stiffness matrix of the ith element in the global coordinate system can be therefore calculated as

$$k^i_{global} = \begin{bmatrix} [t] & \\ & [t] \end{bmatrix}^T k^i_{local} \begin{bmatrix} [t] & \\ & [t] \end{bmatrix}. \quad (17)$$

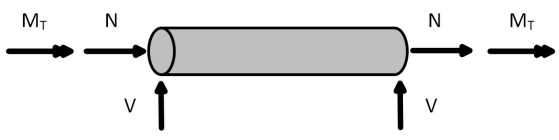

Fig. 3. Degrees of freedom of a beam element

The local mass matrix for the *i*th beam element is given as

$$[m_{local}] = \begin{bmatrix} \frac{\rho A l_e}{3} & 0 & 0 & \frac{\rho A l_e}{6} & 0 & 0 \\ 0 & \frac{78\rho A l_e}{210} & 0 & 0 & \frac{27\rho A l_e}{210} & 0 \\ 0 & 0 & \frac{\rho l_e J}{3} & 0 & 0 & \frac{\rho l_e J}{6} \\ \frac{\rho A l_e}{6} & 0 & 0 & \frac{\rho A l_e}{3} & 0 & 0 \\ 0 & \frac{27\rho A l_e}{210} & 0 & 0 & \frac{78\rho A l_e}{210} & 0 \\ 0 & 0 & \frac{\rho l_e J}{6} & 0 & 0 & \frac{\rho l_e J}{3} \end{bmatrix} \quad (18)$$

where ρ is density.

The global mass matrix is obtained by summing all the global element matrices as follows:

$$M = \sum_{i=1}^{n} m_{global}^{i} \quad (19)$$

where M is the global mass matrix, n is the number of finite elements. The same procedure is followed to construct the global stiffness matrix.

In the transient analysis for a beam with the total n_{dof} degrees of freedom, the equation of motion at time t is formulated as a second order dynamic system:

$$M\ddot{u}(t) + D\dot{u}(t) + Ku(t) = f(t) \quad (20)$$

where $u(t)$ is the n_{dof} dimensional displacement and rotation vector at time t, $\dot{u}(t)$ is the derivative of $u(t)$ with respect to time, $f(t)$ is the external force vector, and M, D and K represent the global mass, damping and stiffness matrices, respectively. The damping matrix D is given as

$$D = \alpha M + \beta K \quad (21)$$

where α and β are the mass- and stiffness-proportional Rayleigh damping coefficients, respectively.

To rewrite the original equation of motion (20) in the first-order form, a state-space representation is used. The state-space representation vector $u(t)$ and its derivative with respect to time $\dot{u}(t)$ are combined into a state vector $x(t)$:

$$x(t) = \begin{bmatrix} u(t) \\ \dot{u}(t) \end{bmatrix}. \quad (22)$$

The state matrix is constructed as in [22]:

$$A = \begin{bmatrix} 0_{[n\times n]} & I_{[n\times n]} \\ -M^{-1}K & -M^{-1}D \end{bmatrix} \quad (23)$$

where $0_{[n\,x\,n]}$ is a zero matrix and $I_{[n\,\times\,n]}$ is an identity matrix. The input matrix is given as

$$B = \begin{bmatrix} 0_{[n\times n]} \\ -M^{-1} \end{bmatrix}. \quad (24)$$

The discrete state transition matrix is given as a matrix exponential

$$\Phi = \exp(A\Delta t) \quad (25)$$

where Δt is the discrete time step. The control matrix is given as

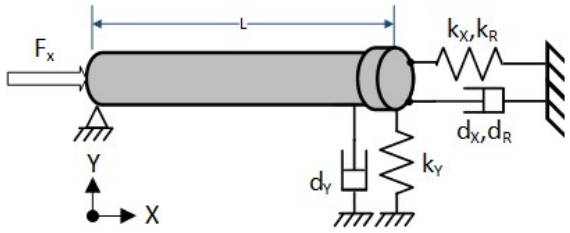

Fig. 4. Boundary conditions of the drill string

$$\Gamma = A^{-1}(\Phi - I)\,B \quad (26)$$

where I is an identity matrix sized $2n \times 2n$. The bit is modelled in the same manner as the beam but with a larger area and elastic modulus.

A. Model Order Reduction

Model order reduction is used to increase the computation speed. The full finite element model with $n_{dof} \times n_{dof}$ matrices is reduced using the normal modes of the conservative homogeneous system. The r first eigenvalues $\lambda_1,\ldots,\lambda_r$ and associated elastic modes $\phi_1,\ldots,\phi_r$ are solutions of the generalized eigenvalue problem:

$$K\phi = \omega^2 M\phi. \quad (27)$$

The elastic mode vectors are united into matrix P, where the elastic modes are columns.

The solution u for the equation of motion (20) is a superposition of the homogeneous solution u_c and particular solution u_p. For the homogeneous solution $f = 0$, and the equation for the particular solution is as follows [23]:

$$M_r\ddot{u}_p(t) + D_r\dot{u}_p(t) + K_r u_p(t) = f_r(t) \quad (28)$$

where $M_r = P^T MP$, $D_r = P^T DP$, $K_r = P^T KP$, $u_p = Pu_r$, $f_r = P^T f$. For the simulation, the reduced matrices M_r, D_r, K_r are used in the state matrix form (23), and the number of eigenvalues is 50.

B. Boundary Conditions

According to a review of drill string vibration models by Ghasemloonia et al. [24], the commonly used axial drill string boundary conditions are fixed at the top–fixed at the bottom, fixed at the top–free at the bottom and equivalent mass–spring–damper at the top and sinusoidal displacement at the bit. The torsional boundary conditions at the top are either constant rotary speed or a control relationship between torque and the rotary speed. The lateral boundary conditions found by Ghasemloonia et al. are free–free; fixed–

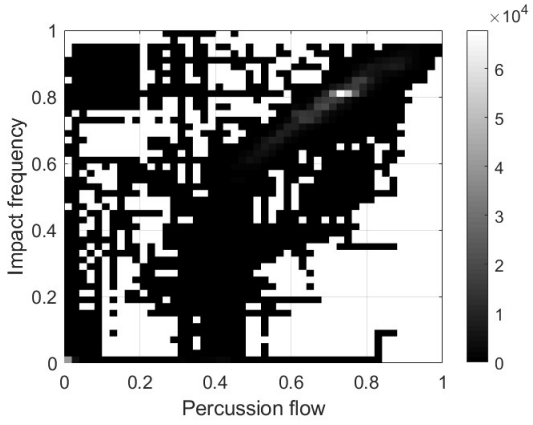

Fig. 5. Correlation between impact piston flow and impact frequency

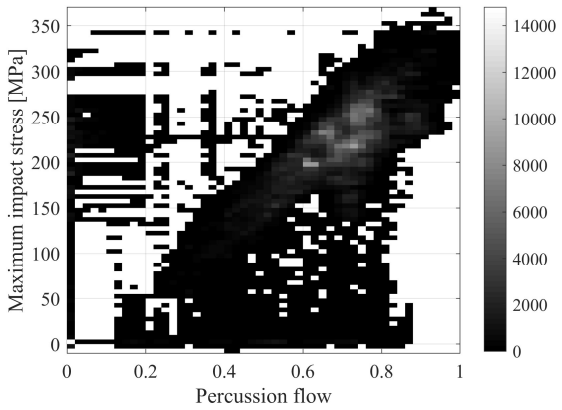

Fig. 6. Correlation between impact piston flow and maximum stress wave amplitude.

free, fixed–fixed; deflected springs and a mass-loaded boundary. Oh et al. [25] used mass–spring–damper as a rock load model in their AMEsim simulation model.

The drill end of the beam is fixed in the vertical direction, a constant rotation speed is assumed, and the impact force acts on the x-direction. The boundary on the bit side of the drill string is assumed to be a spring–damper combination as illustrated in Fig. 4. In practice, the spring and damping boundary condition values are added to the corresponding cells of the stiffness and damping matrices.

C. State Space Scaling

The achieved state space model after model order reduction is scaled using the MATLAB 'prescale' function, which finds the optimal scaling for frequency domain analysis. Scaling is needed since otherwise the state space matrices are heterogeneous in magnitude. Heterogeneity causes a loss of accuracy in computations.

D. Model Parameter Values

The drill rod model parameter values are shown in Table I. The drill rod is made of steel and approximated values for Young's modulus and shear modulus are used.

TABLE I. PARAMETERS OF THE DRILL STRING MODEL

Variable	Value	Unit
A_{bit}	42	cm^2
A_{rod}	17	cm^2
L_{bit}	0.15	m
L_{rod}	3.1	m
n	90	-
E	210	GPa
G	79.3	GPa
J	$1.2791 \cdot 10^{-6}$	m^4
k_X, k_Y, k_R	300	MNm
d_X, d_Y, d_R	$4.63 \cdot 10^6$	-
r	50	-
α	$76.28 \cdot 10^{-8}$	-
β	$156.06 \cdot 10^{-8}$	-
ρ	7850	kg/m^3

E. Percussion Force

Percussive impact force and feed force act on the drill string outside the hole. If the feed force is not sufficient, the drill bit will not be in contact with the rock. Here, it is assumed that feed force is adequate for constant contact.

The measured flow into the impact piston correlates with both the impact frequency (Fig. 5) and the impact amplitude (Fig. 6). These correlations can be used for the simulation of the percussion force amplitude and the impact frequency acting on the drill side of the drill rod. In the simulation, the percussion force profile is achieved using the Repeating Sequence Interpolated block. The amplitude and frequency of the percussion force are varied according to average correlations shown in Figs. 5 and 6.

IV. ROCK MODEL

Rock is modelled as a mass-damper system with additional parameters, including the effect of percussion power and feed force, as in [15]. The cylinder plunger acceleration is calculated as

$$\ddot{x}_c = \frac{c_1(r_{bit})}{m_1}\left(c_1(r_{bit})g_{p1}Q_{perc}p_{perc} + g_{f1}(r_{bit})\Delta p_{feed} + g_{t1}T_M + \left(g_{ft}\frac{\Delta p_{feed}}{T_M}\right) - b_1\dot{x}_c\right) \quad (29)$$

where r_{bit} is the radius of the bit, c_1 is a parameter whose value depends on the radius of the bit, Q_{perc} is the flow to the percussion device, p_{perc} is the percussion pressure, Δp_{feed} is the pressure difference in the cylinder ports ($0.005 \leq 1/T_M \leq 0.024$), and m_1, g_{f1}, g_{t1}, g_{ft} are parameters.

The rotational acceleration is modeled as follows [15]:

$$\dot{\omega} = \frac{1}{a_1}\left(a_2(r_{bit})\left(a_3 + a_4T_M + \frac{1}{a_5p_{perc}} + a_6\Delta p_{feed}\right) - \frac{b_2}{2\pi}\omega\right) \quad (30)$$

where a_1, a_2, a_3, a_4, a_5, a_6 and b_2 are parameters.

The parameter values used for the simulation are displayed in Table II.

TABLE II. ROCK MODEL PARAMETERS

Variable	Value	Unit
a_1	1.8515	$kg \cdot m^2$
a_2	60	m
a_3	13220.8691	$kg \cdot m \cdot s^{-2}$
a_4	10^{-4}	m^{-1}
a_5	10^{-5}	$kg^{-2} \cdot s^4$
a_6	10^{-5}	m^2
b_1	$4.63 \cdot 10^6$	$kg \cdot s^{-1}$
b_2	75	$kg \cdot m^2 \cdot s^{-1}$
c_1	1	-
g_{p1}	$1.5 \cdot 10^{-5}$	$m^{-1} \cdot s$
g_{f1}	$277 \cdot 10^{-5}$	m^2
g_{t1}	$-180 \cdot 10^{-5}$	m^{-1}
m_1	$5/3 \cdot 10^{-5}$	$kg \cdot m^4 \cdot s^{-2}$

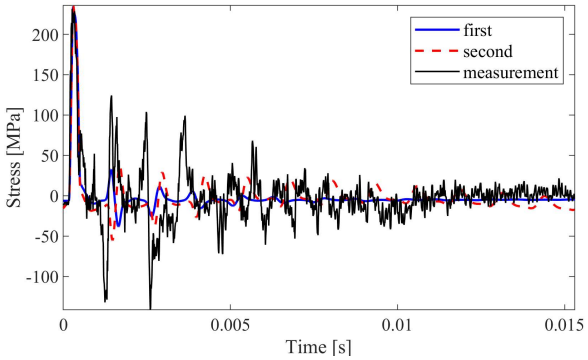

Fig. 7. Simulated stress waves using first lower boundary stiffness value $k_1 = 300$MNm and $d_1 = 4.63 \cdot 10^6$, and for the second wave $k_2 = 1.05k_1$ and $d_2 = 0.9998d_1$.

V. SIMULATION RESULTS

In Fig. 7, two simulated and one measured stress waves are compared. The difference between two simulated stress waves is caused by changed boundary conditions. It is unnecessary to try to achieve exactly the same signal shape as the measured one during the period between the strikes using the described simplified drill string model. Nevertheless, the major parts of the stress wave can be fitted, and the result can be used for control system design purposes. The parameters affecting the stress wave shape are Rayleigh damping

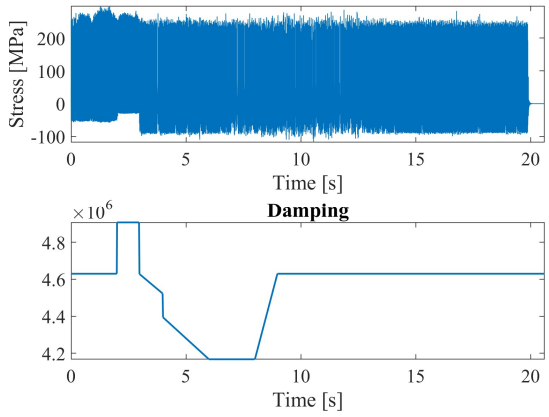

Fig. 8. Stress wave simulation during boundary damping variation

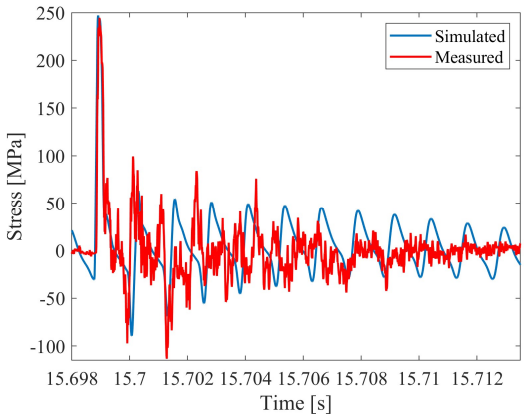

Fig. 9. Stress wave simulation versus measurement

parameters α and β, material parameters, the area of each element, and boundary stiffness and damping parameters.

The simulated stress wave during the drilling of one test hole is shown in Fig. 8. Boundary damping variation during the simulation is shown under the stress wave signal. To vary the simulated percussion force, true values for percussion flow and pressure are inputted into the simulator. The simulation result for the stress wave signal during one impact cycle, zoomed out from Fig. 8 and compared with the measurement, is shown in Fig. 9. On the timescale shown in Fig. 9, the bit–rock boundary values are $k_X = 299.76$ MNm and $d_X = 4.63 \cdot 10^6$. The effect of changing the damping value of the rock to

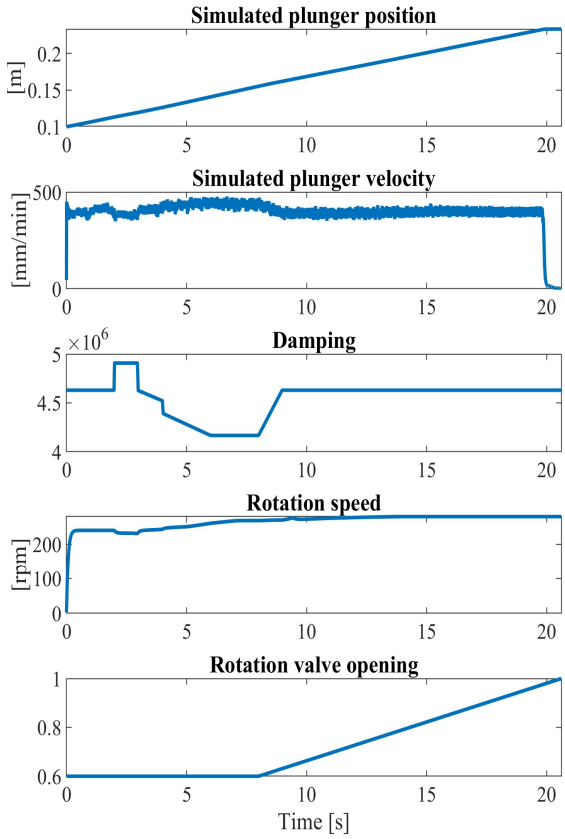

Fig. 10. Simulation results for cylinder plunger position and velocity, and rotation speed when damping value fluctuates.

the simulated position, velocity and rotation speed are shown in Fig. 10. Increasing the damping value decreases the velocity when the drill control parameters remain the same. As simulations can be run using arbitrary inputs and parameters, it is possible to include different controllers in the initial performance testing before testing with the real machine.

VI. Conclusion

Promising simulation results were obtained from modelling a top hammer drill as a combination of feed and rotation circuits, the drill rod as a finite element beam and the bit interaction with the rock. The boundary conditions on the bit side of the drill rod were assumed to be a combination of a spring and a damper, which is a rare choice for finite element modelling. Rock was modelled as a mass–damper system when the penetration rate was estimated.

The next research step is to build an estimator that uses the stress wave signal measurement as an input and provides information about the bit boundary conditions. This information could be directly used for controlling purposes.

Acknowledgment

This research was funded by the Doctoral School of Industry Innovations (DSII) at Tampere University.

References

[1] Heiniö, M., 1999. Rock excavation handbook for civil engineering. Sandvik, Tamrock.

[2] Li, X., Rupert, G., Summers, D. A., Santi, P., and Liu, D., 2000. “Analysis of impact hammer rebound to estimate rock drillability”. Rock Mechanics and Rock Engineering, 33(1), pp. 1–13.

[3] Kahraman, S., 2002. “Correlation of TBM and drilling machine performances with rock brittleness”. Engineering Geology, 65(4), pp. 269–283.

[4] Pavlovskaia, E., Hendry, D. C., and Wiercigroch, M., 2015. “Modelling of high frequency vibro-impact drilling”. International Journal of Mechanical Sciences, 91, pp. 110–119.

[5] Saksala, T., 2013. “3D numerical modelling of bit–rock fracture mechanisms in percussive drilling with a multiple-button bit”. International Journal for Numerical and Analytical Methods in Geomechanics, 37(3), pp. 309–324.

[6] Saksala, T., 2011. “Numerical modelling of bit–rock fracture mechanisms in percussive drilling with a continuum approach”. International Journal for Numerical and Analytical Methods in Geomechanics, 35(13), pp. 1483–1505.

[7] Chiang, L. E., and Elías, D. A., 2008. “A 3D FEM methodology for simulating the impact in rock-drilling hammers”. International Journal of Rock Mechanics and Mining Sciences, 45(5), pp. 701–711.

[8] Saadati, M., 2015. “On the mechanical behavior of granite: Constitutive modeling and application to percussive drilling”. PhD thesis, KTH Royal Institute of Technology.

[9] Liu, H., 2004. “Numerical modelling of the rock fragmentation process by mechanical tools”. PhD thesis, Luleå Tekniska Universitet.

[10] Schunnesson, H., 1998. “Rock characterisation using percussive drilling”. International Journal of Rock Mechanics and Mining Sciences, 35(6), pp. 711–725.

[11] Franca, L. F., 2011. “A bit–rock interaction model for rotary–percussive drilling”. International Journal of Rock Mechanics and Mining Sciences, 48(5), pp. 827–835.

[12] Pettersson, H., Krus, P., and Palmberg, J.-O., 1997. “Simulation of a reciprocating rock drill and drill rod impact”. In The 5th Scandinavian International Conference on Fluid Power, SICFP, Vol. 97.

[13] Aarsnes, U. J., and Wouw, N., 2018. “Dynamics of a distributed drill string system: Characteristic parameters and stability maps”. Journal of Sound and Vibration, 417, 03, pp. 376–412.

[14] Silveira, M., and Wiercigroch, M., 2009. “Low dimensional models for stick-slip vibration of drill-strings”. Journal of Physics: Conference Series, 181, aug, p. 012056.

[15] Peltokangas, S., Launis, S., Saarela, M., and Mattila, J., 2017. “Modeling and simulation of a hydraulic drill for control system design purposes”. In ASME/Bath 2017 Fluid Power and Motion Control, FPMC2017, ASME.

[16] Krus, P., and Linköping University. Department of Mechanical Engineering, D. o. F. P. C., 1988. “On load sensing fluid power systems: with special reference to dynamic properties and control aspects”. PhD thesis.

[17] Palmberg, J.-O., Krus, P., and Kang-Zhi, D., 1985. “Dynamic response characteristics of pressure-control pumps”. In Proceedings, First International Conference on Fluid Power Transmission and Control.

[18] Palmberg, J.-O., and Kang-Zhi, D., 1987. “Modelling and simulation of pressure-controlled pumps”. International Journal of Modelling and Simulation, 7(4), pp. 153–158.

[19] Bak, M. K., and Hansen, M. R., 2012. Modeling, performance testing and parameter identification of pressure compensated proportional directional control valves. Fluid Power Net International PhD Symposium. Fluid Power Net International, pp. 889–908.

[20] Ellman, A., and Piché, R., 1996. A modified orifice flow formula for numerical simulation. ASME Press, pp. 59–62.

[21] Canudas-de Wit, C., Olsson, H., Astrom, K. J., and Lischinsky, P., 1995. “A new model for control of systems with friction”. IEEE Transactions on Automatic Control, 40(3), pp. 419–425.

[22] Kwon, Y., and Bang, H., 2000. The finite element method using MATLAB. Mechanical and Aerospace Engineering Series. CRC Press.

[23] Yoo, E. J., 2010. “Parametric model order reduction for structural analysis and control”. Dissertation, Technische Universität München, München.

[24] Ghasemloonia, A., Rideout, D. G., and Butt, S. D., 2015. “A review of drillstring vibration modeling and suppression methods”. Journal of Petroleum Science and Engineering, 131, pp. 150 – 164.

[25] Oh, J.-Y., Lee, G.-H., Kang, H.-S., and Song, C.-S., 2012. “Modeling and performance analysis of rock drill drifters for rock stiffness”. International Journal of Precision Engineering and Manufacturing